



Dependence of TiO₂ nanotube microstructural and electronic properties on water splitting



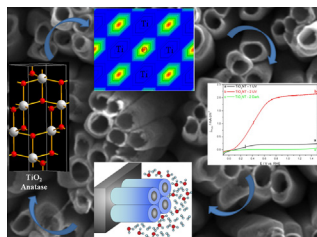
R.G. Freitas, M.A. Santanna, E.C. Pereira*

NANOFAEL—LIEC, Departamento de Química, Universidade Federal de São Carlos, C.P.: 676, CEP, 13565-905 São Carlos, SP, Brazil

HIGHLIGHTS

- TiO₂NT were prepared by electrochemical anodization.
- Different tube diameters (50.8 nm and 70.5 nm) were obtained.
- Photocurrent density increase 925%.
- Crystallite size related to boundary crystallite region and associated to recombination center.

GRAPHICAL ABSTRACT



ARTICLE INFO

Article history:

Received 20 September 2013

Received in revised form

20 November 2013

Accepted 21 November 2013

Available online 2 December 2013

Keywords:

TiO₂ nanotube

Crystallite size

Lattice strain

Water splitting

ABSTRACT

In this work, TiO₂ nanotubes were prepared by anodization in ionic liquid at 10 °C and 20 °C. Different tube diameters (50.8 nm and 70.5 nm) were obtained, and both of them exhibited an anatase phase with distinct crystallite sizes and lattice strains. The increase in the crystallite size led to a decrease in the grain boundary surface area, which could be associated with the recombination centers of the photo-generated charge carriers. Electrochemical impedance spectroscopy was used to correlate the water splitting photoactivity with the charge transfer resistance and the apparent roughness. A schematic representation of the nanotube structures consisting of two layers, compact and porous, proved to be appropriate to clarify the obtained results.

© 2013 Elsevier B.V. All rights reserved.

1. Introduction

There is more than enough solar radiation all over the world to satisfy the vast increase in the demand for solar power. Sunlight that reaches the Earth's surface is enough to provide 28,500-times as much energy as we can currently use [1]. Globally, each square meter of land is exposed to enough sunlight to produce 1700 kWh year⁻¹ on average [1]. Therefore, it is worthwhile to provide new photoelectrochemical (PEC) materials that are capable

of converting chemical energy into electricity using the solar radiation.

The key to a hydrogen economy is to find an efficient and inexpensive method to generate hydrogen on a renewable basis (i.e. without the use of fossil fuel). Therefore, a PEC system that combines the harvesting of solar energy with the electrolysis of water is able to generate hydrogen and oxygen that can be used in different electrochemical devices to convert energy. There are several semiconductors that have been studied for use as PEC systems for water splitting, but the major challenges for the solar production of hydrogen are in finding a material that shows: i) chemical stability, ii) narrow band gap, and iii) appropriate band edge positions.

Promising materials for solar energy conversion must combine ordered structure, highly tunable electronic properties, high

* Corresponding author. Tel./fax: +55 16 3351 8214.

E-mail addresses: ernesto@ufscar.br, ernestopereira51@gmail.com (E.C. Pereira).

specific surface area, confined charge transport, and hydrophilic surface properties. TiO₂ nanotubes (TiO₂NTs) emerged as a promising class of semiconductors that are able to combine the desired features mentioned above.

In recent years [2], non-aqueous systems, such as ionic liquids, have attracted a high technological and scientific interest as they represent a group of solvents that consist only of ions and remain in the liquid state at low temperatures (<100 °C). Also, TiO₂NT obtained in ionic liquid is considered the third TiO₂NT generation. During TiO₂NTs synthesis, the use of ionic liquids (IL) as electrolytes is a very recent procedure, with few papers reporting their use. Schmuki et al. [2] observed the formation of well-ordered self-organized TiO₂NTs produced in 1-butyl-3-methyl-imidazolium-tetrafluoroborate (BMIM-BF₄) IL. Misra et al. [3] synthesized double-walled vertically oriented TiO₂NTs using sonoelectrochemical anodization in BMIM-BF₄ and observed the formation of concentric nanotubes, as well as an enhancement in the rate of water splitting. Teixeira et al. [4] also prepared TiO₂NTs in BMIM-BF₄, and observed the improvement in water splitting. Finally, TiO₂NTs synthesized in BMIM-BF₄ can be used as an anode for Li⁺ intercalation [5,6].

This study was motivated by the fact that, while ILs are promising electrolytes for TiO₂NT synthesis, there is a lack of studies exploring the correlation of electrochemical impedance with the physical properties and their effects on water splitting. Therefore, in this study, we report the use of TiO₂NTs, prepared using IL electrolytes, for the water splitting reaction, combining electrochemical impedance studies and correlating the observed results with the crystalline structures obtained. To the best of our knowledge, such an approach has not yet been described elsewhere in the literature.

2. Experimental

2.1. Electrode preparation

TiO₂NT arrays were prepared by anodizing titanium foils (99.8% Alfa Aesar) with 1.0 cm² of exposed area in electrolytes composed of ethylene glycol (Synth; 85 vol.%), water purified by reverse osmosis (10 vol.%), and 1-butyl-3-methyl-imidazolium-tetrafluoroborate (BMIM-BF₄; Sigma Aldrich; 5 vol.%). Prior to each anodization, Ti samples were ultrasonicated in acetone, rinsed with distilled water, and dried in a N₂ stream. Anodization was performed at 10 °C or 20 °C (referred to as TiO₂NT-1 and -2, respectively) using a standard two-electrode cell with the Ti foil as the anode and a platinum foil (4.0 cm²) as the cathode. The temperature was kept constant using a thermostatically controlled water bath (Quimis-Q214S).

The reaction was conducted using a two-step procedure: i) the voltage was swept from the open circuit potential to a maximum of 80 V at $v = 0.1 \text{ V s}^{-1}$, and ii) maintained at 80 V for 240 min using a Keithley-2410 sourcemeter. After anodization, the samples were rinsed with distilled water and thermally treated at 450 °C for 120 min to eliminate any water, improve its mechanical stability, and to obtain the TiO₂-anatase crystalline structure phase. Then, the samples were cooled at a rate of 5 °C min⁻¹.

2.2. Electrode characterization

The TiO₂NTs morphological characterization was carried out using a Supra 35 Zeiss Field Emission Scanning Electron Microscope. The optical absorption spectra were obtained using a UV-Vis spectrometer (UV-Vis DRS; Cary 5G).

The X-ray diffraction (XRD) patterns were obtained using a Siemens diffractometer model D-5000 with CuK α radiation and $\lambda = 1.5406 \text{ \AA}$. To obtain the microstructural data of the TiO₂NT

electrodes, a Rietveld refinement [7] was performed using the General Structure Analysis System (GSAS) program [8] suite with the EXPGUI interface [9]. The original Rietveld formulation, and many of its successors [10], considers the diffraction line width as a smooth function of the d -spacing of the diffraction angle (2θ), whereas many peaks of interest near 2θ have very different widths. Hence, in this work, the peak profile function developed by Stephens [11] was used to model the experimental data. In this method, considerations are made for diffraction widths that are not a smooth function of d , which might arise from anisotropic sample size broadening or from a particular pattern of defects (e.g. stacking faults). Finally, the bi-dimensional model for the crystallite size described by Larson and von Dreele [8] was used to account for the anisotropy in the half width of the reflections.

The electron density maps were calculated following the method described in detail previously [12]. In brief, a point (x, y, z) of the crystallite cell with volume (V) was calculated by the Fourier series using the structural factors $F(h, k, l)$

$$\rho(x, y, z) = V^{-1} \sum_h \sum_k \sum_l F(h, k, l) \exp[2\pi i(hx, ky, lz)] \quad (1)$$

where (x, y, z) represents a vector (r) of real space, with one vector space (a, b, c) and another vector (h, k, l), which represent the coordinates of one vector from the reciprocal space with base (a^*, b^*, c^*), i.e. they are the coordinates from the diffraction plane that it is given by Bragg's Law. The electron density distribution in the base plane {slice 1 with $Z = 0$ (i.e. face ab), with a set (hkl) as the projection plane (001)} were calculated by GSAS program [8] from XRD data for both TiO₂NTs.

All electrochemical water splitting measurements were performed in a three-electrode configuration using a reversible hydrogen electrode (RHE), a counter electrode of platinum wire, and a TiO₂NTs electrode as the photoanode. The measurements were performed in 0.5 M H₂SO₄ with an ultraviolet UV lamp housing (Newport Oriel Instrument model 66881 QTH).

Electrochemical impedance spectroscopy (EIS) was measured with an excitation signal of 5 mV in the frequency range from 10 KHz to 0.01 Hz using an Echochimie Autolab PGSTAT 30. Before each experiment, the electrodes were polarized at several potentials for 5 min to reach the steady state. The impedance data analysis was performed with the ZView 3.1 software package, where the spectra were fitted by means of a complex, non-linear, least-squares procedure.

3. Results and discussion

3.1. Morphological and structural characterization

In order to obtain more information about the morphology, FESEM images were acquired for TiO₂NT photoelectrodes, as shown in Fig. 1.

The average tube diameter reached was $50.8 \pm 9.5 \text{ nm}$ and $70.5 \pm 8.5 \text{ nm}$ for samples obtained at 10 °C and 20 °C, respectively. Teixeira et al. [4] and Schmuki et al. [2] prepared TiO₂NTs in BMIM-BF₄ IL, and observed tube diameters around 80 nm and 43 nm, respectively. Although the TiO₂NT morphology exhibited in Fig. 1b is the most common found in the literature [13,14], the TiO₂NT patch-like bundle morphology, such as that shown in Fig. 1a, has been also shown [15]. Schmuki et al. [2] also described such morphology using BMIM-BF₄ IL and 0.15 vol.% water content, as did Shankar et al. [16] and Liang et al. [17] for TiO₂NTs synthesized in 0.25 vol.% HF + 1 vol.% H₂O in diethylene glycol and 1 vol.% HF in dimethyl sulfoxide, respectively. Moreover, Lin et al. [18] observed similar TiO₂NT morphologies using 20 vol.% H₂O + 0.5 vol.% NH₄F in

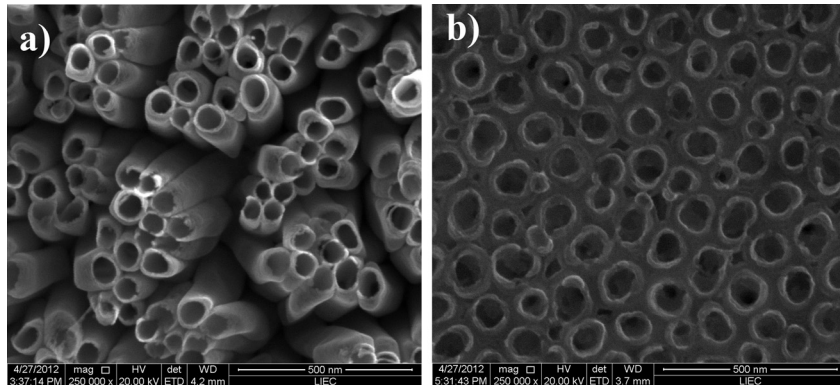


Fig. 1. FESEM images of TiO_2 films formed from a Ti foil at a) $10\text{ }^\circ\text{C}$ and b) $20\text{ }^\circ\text{C}$. $E_{\text{appl}} = 80\text{ V}$.

ethylene glycol. According to Schmuki et al. [2], this morphology reflects the passivating action of water. Furthermore, it could be related to a significant variation in the electrolyte conductivity due to the high viscosity of ethylene glycol. At the cold temperature used ($10\text{ }^\circ\text{C}$), the low concentration of ionic charge carriers (i.e. F^-) and the large hydrodynamic radius of the dissociated ions are due to solvation by water and ethylene glycol molecules. All of these factors are more evident at low temperatures, as shown in Fig. 1a. These results are in agreement with Shankar et al. [16].

Finally, Fig. 1a and b shows that the temperature increase leads to a larger tube diameter during the anodization process. According to Macak and Schmuki [19], the strong dependence of the results on the electrolyte temperature indicates that the dominant growth limiting factor is diffusion of the fluoride species to the pore tip or of the reaction products away from the tip. It is reasonable, once that temperature and diffusion coefficient have a linear dependence according to the Stokes–Einstein Equation [19]. Therefore, the increase in the temperature leads to an increasing in the fluoride species diffusion coefficient toward the nanotubes arrays. Xie and Blackwood [20] studied the formation of TiO_2NT in ethylene glycol medium, and observed an increase in the tube diameter at temperatures from $10\text{ }^\circ\text{C}$ up to $20\text{ }^\circ\text{C}$. This is also in agreement with previous reports [21].

The band gap (E_g) was estimated using the Tauc–Wood equation [22]

$$(\alpha h\nu)^s = h\nu - E_g \quad (2)$$

where α is the absorption coefficient, and $h\nu$ and E_g are photon energy and optical band-gap energy, respectively. The value used for s was 0.5 once TiO_2 was classified as an indirect gap semiconductor. E_g values were then determined by extrapolation of the linear portion of the $(\alpha h\nu)^s$ curve versus the photon energy ($h\nu$) to $(\alpha h\nu)^s = 0$. For the TiO_2 electronic properties of the relevant energy levels that form the band edges and, thus, define the band gap, are considered to be the $\text{Ti}3d$ states and $\text{O}2p$ levels. The lowest empty energy levels are $\text{Ti}3d_{xy}$ and are representative of the conduction band (CB) edge, whereas the full $\text{O}2p$ states, particularly the nonbonding $p\pi$ states, define the valence band (VB). Both anatase and rutile show this general distribution of states [23,24]. Additionally, the linear dependence of $(\alpha h\nu)^{0.5}$ on $h\nu$ indicates that TiO_2 is essentially an indirect-transition-type semiconductor. The straight-line portion of the curve, when extrapolated to zero, gives the optical band gap (E_g).

Fig. 2 shows that different anodization temperatures lead to distinct band-gap values. These values were 2.95 eV and 2.8 eV for $\text{TiO}_2\text{NT-1}$ and -2, respectively. Therefore, higher anodization

temperatures lead to lower band-gap values. The reported band-gap value of the anatase phase in bulk is 3.2 eV [25], and distinct morphologies related to the nanotubes structures can lead to different band-gap values. According to Grimes and Mor [26], a slight blue shift in the value (i.e. $\text{TiO}_2\text{NT-2}$) might be due to a quantization effect in the nanotubular structure [26]. The degree of lattice distortion is likely to be relatively higher for nanotubes array films, thus causing aggregation of vacancies acting as trap states along the seams of nanotube walls leading to a lower band-to-band transition energy.

From Fig. 3, it was concluded that a large amount of anatase phase was present in these samples, which was characterized by the diffraction peaks at $2\theta = 25.281$ (101), $2\theta = 36.946$ (103), $2\theta = 37.800$ (004), and $2\theta = 48.049$ (200) (JCPDS 21–1272). The TiO_2NT self-ordered film was very thin, since titanium peaks, rather than anatase– TiO_2 peaks, were observed (JCPDS 44–1294) at higher intensities. Also, small contributions of rutile– TiO_2 crystalline phase at $2\theta = 27.446$ (110) and $2\theta = 36.085$ (101) (JCPDS 21–1276) were observed.

The results obtained by the Rietveld refinement method (Fig. 3) indicate a good agreement between the observed XRD patterns and the theoretical results. Moreover, the difference between the experimental XRD profile patterns observed and the theoretical calculated data showed differences close to zero in the scale of

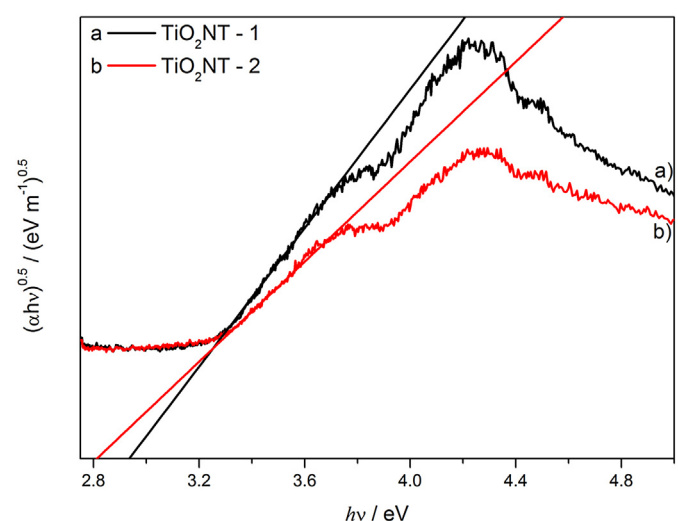


Fig. 2. Band-gap energy plot for all of the TiO_2 nanotubes photoelectrodes we prepared.

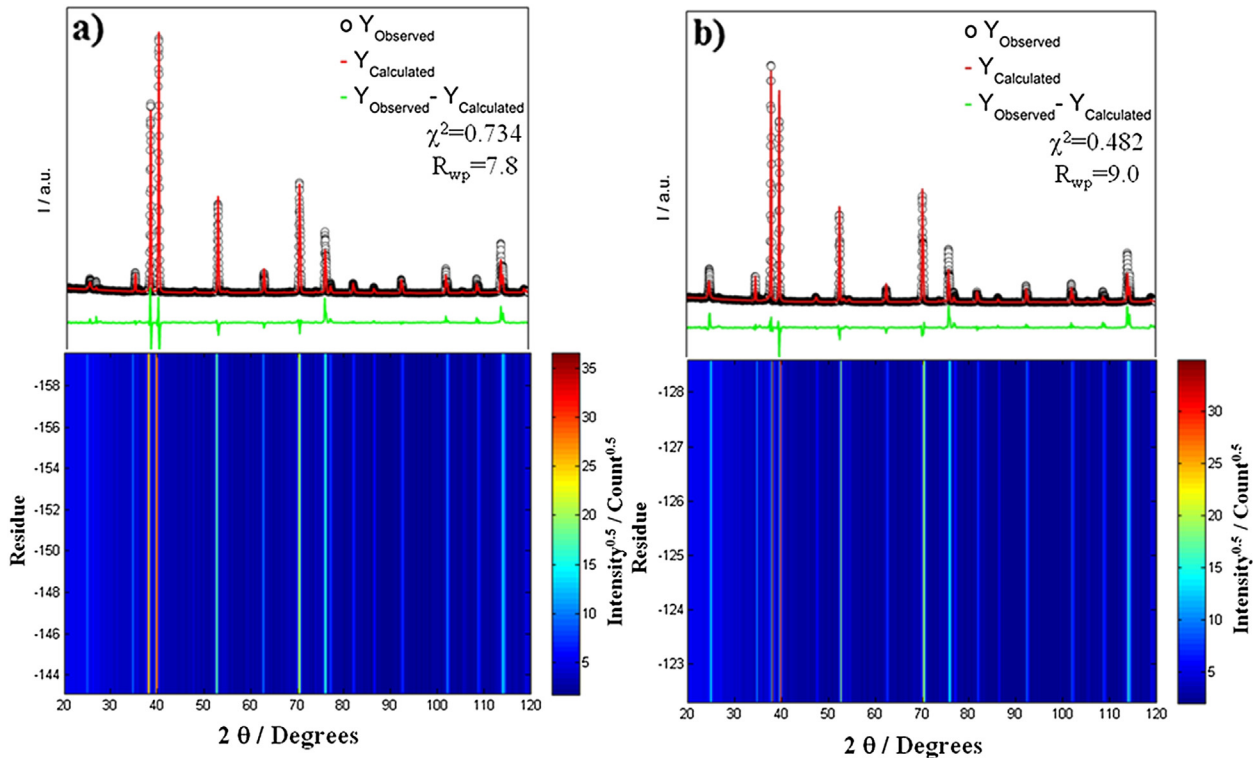


Fig. 3. Rietveld refinement plot and 2D multiplot (residuals) of PMO TiO₂NT photoelectrodes prepared at a) 10 °C and b) 20 °C.

intensity, as illustrated by a line ($Y_{\text{observed}} - Y_{\text{calculated}}$). The 2D XRD multiplot (residuals) is indicated by colors (Fig. 3a and b). The Rietveld method is a least-squares refinement procedure, where the experimental step-scanned values are adapted to the calculated values.

The quality of the structural refinement data is acceptable when the weighted index (R_{wp}) is $R_{wp} < 10\%$ [8] and the discrepancy between the observed values and the values expected under the model in question (χ^2) are lower than two [8]. Therefore, it was possible to observe that the Rietveld refinement evaluated for TiO₂NT-1 and -2 was in agreement with the Rietveld procedure. Crystalline size (CS) and lattice strain (S) were among the parameters that could be obtained from the Rietveld analysis.

The values obtained for CS were 25.0 nm and 33.0 nm for the TiO₂NT-1 and -2 photoelectrodes, respectively. The CS increased when obtained at the higher anodization temperature. These values were similar to those reported in the literature [27] for TiO₂NT electrodes. Sung et al. [27] prepared TiO₂NTs by electrochemical anodization in order to use them in solid state dye-sensitized solar cell devices. According to the authors, the average of crystalline sized obtained was 35.2 nm.

The lattice strains calculated were 1.25% and 0.35% for TiO₂NT-1 and -2, respectively. These positive values were related to the tensile strain on the nanotubes structures, and TiO₂NTs prepared at a lower anodization temperature experienced higher tensile strain. Mathew et al. [28] studied the deposition of thin TiO₂ films onto a glass substrate. They observed values for tensile strain around 0.27% for samples annealed at 450 °C, and there was an increase in these values for at lower annealing temperature. The effect of tensile strain observed for TiO₂NTs is shown in Fig. 4.

Fig. 4 shows the crystallographic parameter obtained from previous Rietveld refinement, described above. The average volume of the anatase unit cell increased from 135.35 Å³ to 136.14 Å³ for the higher anodization temperature, thus leading to an increase in the

CS and a decrease in the lattice strain. Such an increase in the volume was related to the preferential orientation in the *c*-axis, which increased from 9.424 Å to 9.4836 Å for the higher anodization temperature, and such values are in agreement with previous reports. According to the crystallographic information file (CIF-202242-ICSD) obtained for TiO₂–anatase phase (I 41/and – 141), the *a*- and *c*-axis we obtained were 3.7847 Å and 9.5123 Å, respectively. Xiong et al. [29] studied the preparation of TiO₂–anatase by the sol–gel technique and observed *a* = 3.7852 Å and *c* = 9.5139 Å. Fan et al. [30] studied the effect of iron ions on the anatase–rutile transition phase. The values of *a*- and *c*-axis were from 3.7986–3.8030 Å to 9.4914–9.5600 Å, respectively. Sen et al. [31] studied the transformation of ball milled anatase–TiO₂ using Rietveld refinement. According to the authors, from 0 h to 100 h during the milling procedure, the *a*- and *c*-axis changed from 3.788–3.786 Å and 9.520 Å to 9.527 Å, respectively. Therefore, Sen et al. [31] also observed a preferential increase along the *x*-axis, as reported above. Finally, the values obtained in this study are in agreement with those obtained using Rietveld refinement [32,33].

3.2. Photoelectrochemical characterization

The photooxidation activity of the TiO₂NT photoelectrodes was also evaluated by measuring the photocurrent for the water splitting reaction using linear sweep voltammetry (LSV). Fig. 5 shows the typical photocurrent versus the measured potential for TiO₂NT-1 and -2 photoelectrodes under UV-illumination. The results are also shown for the LSV for one of the samples under dark conditions in order to measure any current leakage. Anodic photocurrent was clearly observed, and it is reasonable that the generated anodic photocurrent increases with the increase in the applied potential, once the *n*-type semiconductor was used as the photoanode.

The first-derivative method [34] is the most accurate calculation method to determine the onset potential. Using this procedure, we

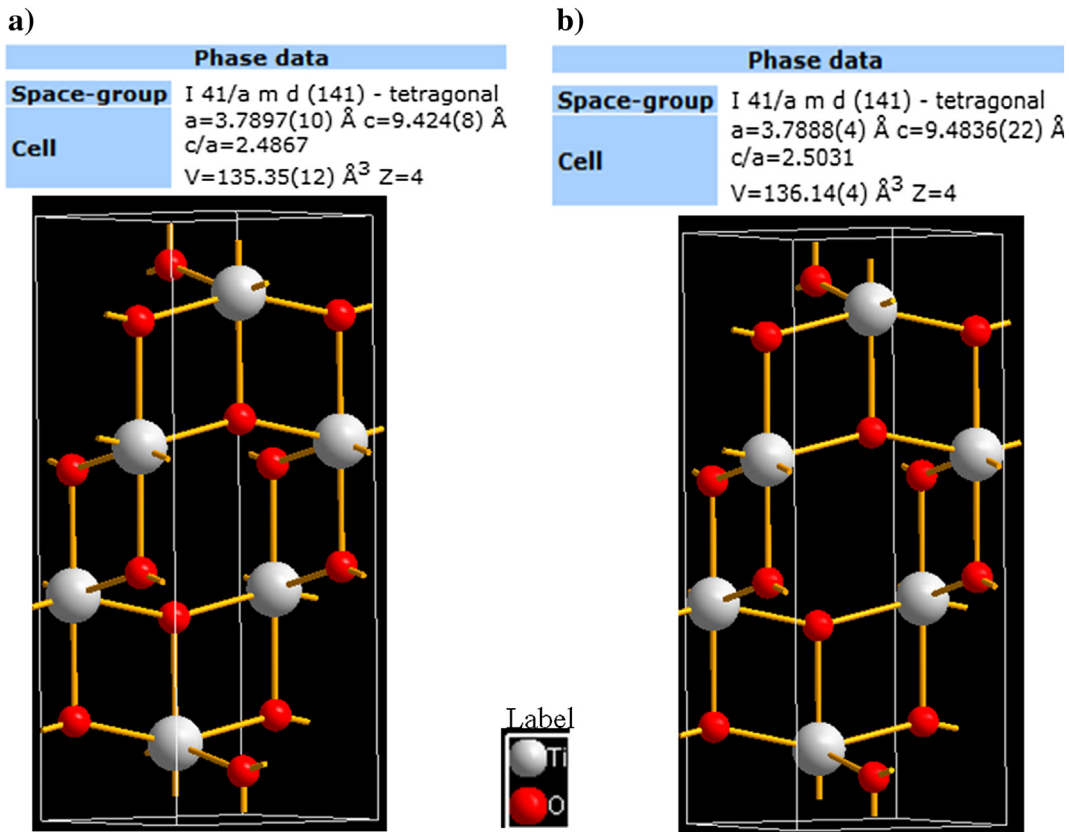


Fig. 4. The crystalline structure the TiO_2 -anatase unit cell obtained for a) $\text{TiO}_2\text{NT-1}$ and b) $\text{TiO}_2\text{NT-2}$ photoelectrodes.

observed that the onset potential shifted 140 mV toward the negative potential for $\text{TiO}_2\text{NT-2}$ when compared to the $\text{TiO}_2\text{NT-1}$ photoelectrode. Also, the peak photocurrent density increases 925% for $\text{TiO}_2\text{NT-2}$ when compared to $\text{TiO}_2\text{NT-1}$. The higher photoelectrocatalytic activity for $\text{TiO}_2\text{NT-2}$ could be related to its lower band-gap values (Fig. 2), higher CS, and lower lattice strain (Figs. 3 and 4) when compared to $\text{TiO}_2\text{NT-1}$. Pereira et al. [35] prepared TiO_2 thin film under galvanostatic conditions for dye degradation. They observed that, although the band gap did not have a significant

impact on photocatalysis, the photoactivity was governed by the crystalline microstructure. According to the authors, a higher CS led to a decrease in the boundary crystallite region, which could be associated with recombination centers of photogenerated charge carriers. Shrivastav et al. [36] also studied the water splitting reaction on nanocrystalline $\text{Zn}_{1-x}\text{Ru}_x\text{O}$ thin films. The authors prepared nanoparticles in the 29–52 nm range, and observed an increase in the photocurrent up to 2300% for larger nanoparticles when compared to the smallest [36]. Therefore, the higher photoactivity observed for TiO_2NT photoelectrode can be attributed to the increase in the carrier mobility in the samples.

Electrochemical impedance spectroscopy is a powerful technique for studying reactions involving charge transfer. Fig. 6 shows a Nyquist spectra for $\text{TiO}_2\text{NT-1}$ and -2 under illumination. The lower charge transfer resistance was exhibited by $\text{TiO}_2\text{NT-2}$ and is in agreement with its higher photoactivity shown in Fig. 5.

We observed a pseudocapacitive behavior, with a time constant at low frequency and another one at high frequency region (Fig. 6, left inset). These spectra were fitted with analogous equivalent circuits reported in the literature for TiO_2NTs photoelectrodes [37]. Ho et al. [38] studied TiO_2NTs infiltrated with TiO_2 nanoparticles using a dipping-rising-hydrolysis process for dye-sensitized solar cell applications. The authors clearly observed two semicircles in the Nyquist spectra. However, they used the transmission line approach developed by Bisquert [39] to fit their spectra.

TiO_2NTs are described as the result of two-film structure formed by compact base layers, constituted by the oxide film not interested by the nanotubular structure, and a porous overlayer, where nanotubes are fully developed. Therefore, two RQ elements are needed in the equivalent circuit to take into account the capacitive–resistive processes occurring at the interface of the two layers

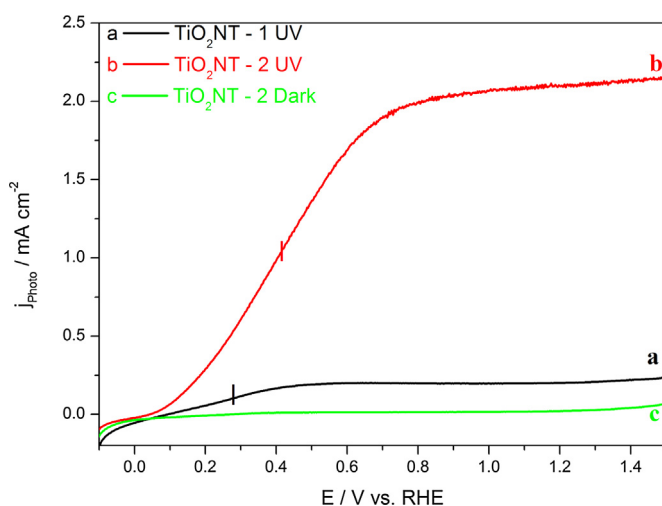


Fig. 5. Linear sweep voltammetry (LSV) obtained for TiO_2NT photoelectrodes in 0.5 M H_2SO_4 and a UV lamp housing. $T = 25^\circ\text{C}$.

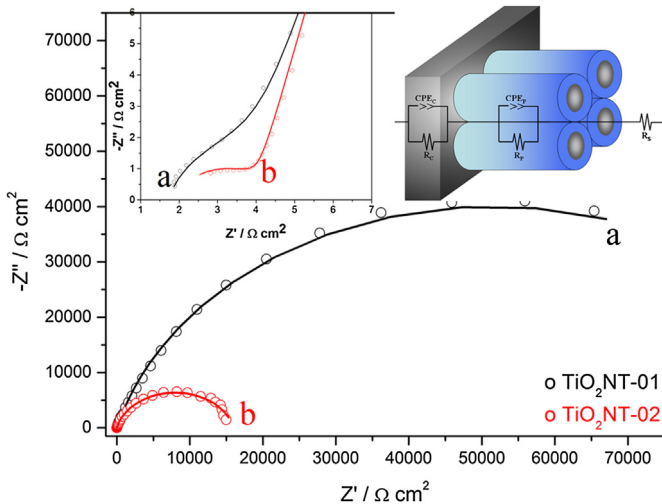


Fig. 6. Complex plane plots for TiO_2NT photoelectrodes in 0.5 M H_2SO_4 and a UV lamp housing, $T = 25^\circ\text{C}$. Left inset: high frequency observed, and right inset: equivalent circuit elements used in the complex non-linear least-squares procedure.

(Fig. 6, right inset). In this model, the behavior of the porous layer was associated with the RQ circuit element with the lowest value of resistance, and the RQ circuit element with higher resistance has been associated with the compact layer. All of the charge transfer resistance along the LSV is shown in Fig. 7.

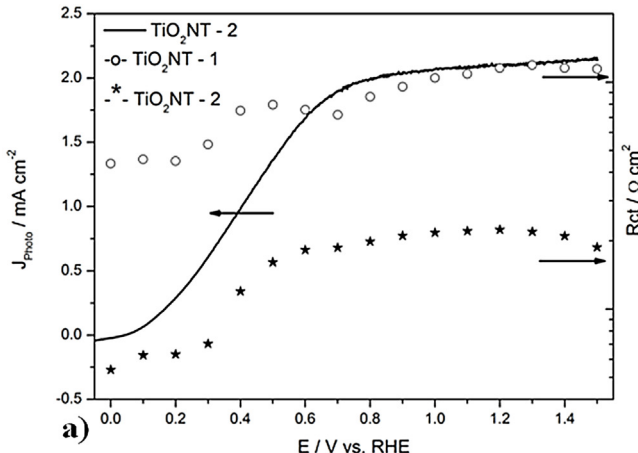


Fig. 7a shows that the charge transfer resistance related to $\text{TiO}_2\text{NT-2}$ was lower than that observed for $\text{TiO}_2\text{NT-1}$ photoelectrodes along all LSVs. Moreover, the charge transfer resistance for the $\text{TiO}_2\text{NT-1}$ and -2 photoelectrodes attained a plateau at potentials similar to the water splitting LSV (i.e. 0.7 V), indicating a higher stability at higher anodic potentials.

The change in the apparent roughness for $\text{TiO}_2\text{NT-1}$ and -2 along the water splitting LSV is shown in Fig. 7b. $\text{TiO}_2\text{NT-2}$ photoelectrodes exhibited lower apparent roughness along all LSV when compared to $\text{TiO}_2\text{NT-1}$ photoelectrodes, which was likely related to the patch-like bundle morphology of $\text{TiO}_2\text{NT-1}$. Furthermore, the potential associated with the peak photocurrent density occurs within the same potential range (i.e. 0.7–0.8 V) where higher apparent roughness was observed. This means that the increase in the photocurrent values led to the higher apparent roughness values.

Based on all of the data previously discussed, a pictorial electrochemical view of the process at the TiO_2NT –electrolyte interface can be regarded in Fig. 7c and d. Once that current is the kinetic measurement of an electrochemical process, at lower overpotential, the photocurrent is lowest and the apparent roughness is the lowest observed. As a result of the increase in the overpotential values, the photocurrent increases and, consequently, the rate related to water splitting, increased, leading to higher oxygen yields on these TiO_2NT photoelectrodes. Therefore, under these conditions, the highest values for the apparent roughness were obtained, as shown in Fig. 7d.

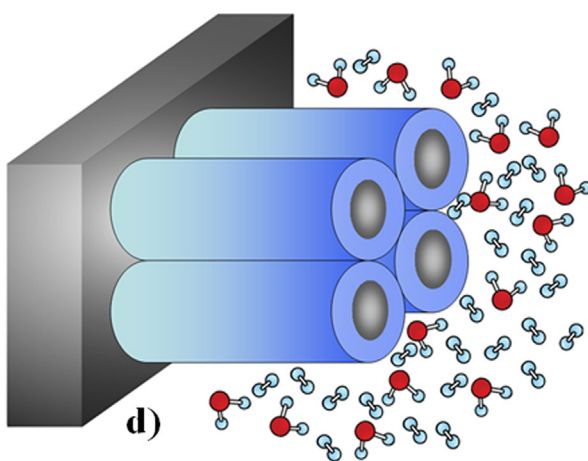
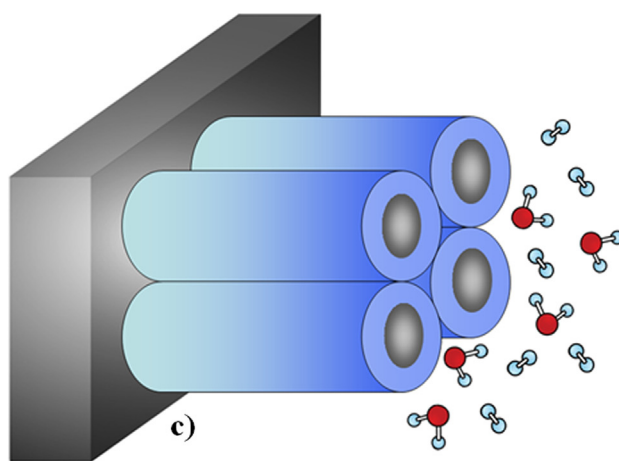
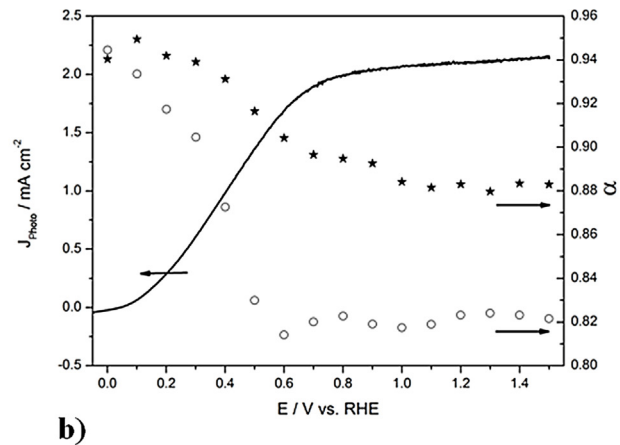


Fig. 7. The relationship between linear sweep voltammetry (LSV) obtained for $\text{TiO}_2\text{NT-2}$ photoelectrodes for a) charge transfer resistance and b) apparent roughness factor. Pictorial representation of the water splitting reaction at the c) lower applied potential and d) higher applied potential.

3.3. Electronic state characterization

Electronic density of states is one of the most accurate parameter that the crystallite size [40] and lattice strain [41,42] can modulate.

When a voltage variation (dV) is applied to the conductive substrate of the nanostructured film, the Fermi level is displaced, as described by $dE_{Fn} = -q dV$ (where q is the elementary charge). Consequently, the electron density changes by a quantity (d_n). Jamnik and Maier [43] studied the mass and charge transport using a generalized equivalent circuit and found the electrochemical capacitance (per unit of volume) was associated with the change in the number density of the electrons (n) to the change in the electrochemical potential.

$$C_\mu = q \frac{d_n}{dE_{Fn}} \quad (3)$$

Also, the chemical capacitance (C_μ) reflects the change in the electron density for a small variation in the chemical potential. For a given Fermi level, the equation has the following form [44,45]:

$$C_\mu = e^2 \frac{\partial}{\partial E_F} \int_{E_1}^{E_2} F(E - E_{Fn}) g(E) dE \approx e^2 g(E_F) \quad (4)$$

where $F(E - E_{Fn})$ is the occupation factor given by the Fermi–Dirac distribution function and $g(E)$ is the density of states. According to Bisquert et al. [46], a common finding in nanostructured TiO_2 is an exponential distribution of the localized states in the band gap, as described by the expression

$$g(E) = \frac{N_L}{k_B T_0} \exp[(E - E_c)/k_B T_0] \quad (5)$$

where N_L is the total density of the localized states and T_0 is a parameter with temperature units that determines the depth of the distribution below the lower edge of the conduction band (E_c). Finally, the most successful model for describing transport in photoconductor is a Gaussian disorder model, developed by Bassler [47], using a regular array of hopping sites with a Gaussian distribution of site energy and developed using a Monte Carlo simulation

$$g(E) = \frac{N}{\sqrt{2\pi}\sigma} \exp\left[-\frac{(E_0 - E)^2}{2\sigma^2}\right] \quad (6)$$

where N accounts for the total density of states (DOS) with a mean energy (E_0) and width (σ). The distribution of the DOS is broad if $\sigma > k_B T$. According to Bisquert et al. [48,49], it is widely accepted that the distribution of electronic states in disordered photoconductors has a Gaussian shape, as is shown by capacitance measurements [48,49]. In the case of organic semiconductors, the Gaussian distribution results from the fluctuation of the lattice polarization energies [47], dipole interactions [50], and molecular geometry fluctuations [51]. The calculated DOS for $\text{TiO}_2\text{NT-1}$ and -2 photoanodes is shown Fig. 8, where they are plotted versus the reversible hydrogen electrode.

The Gaussian DOS resulting from the fits of several cells are centered at $E_0 = 0.92$ V and 0.95 V for $\text{TiO}_2\text{NT-1}$ and -2, respectively. It is interesting to note that such values coincide with the plateau of the higher density photocurrent shown in Fig. 5.

The disorder parameters (σ_i) obtained were 648 meV and 488 meV for $\text{TiO}_2\text{NT-1}$ and -2, respectively. In general, weak

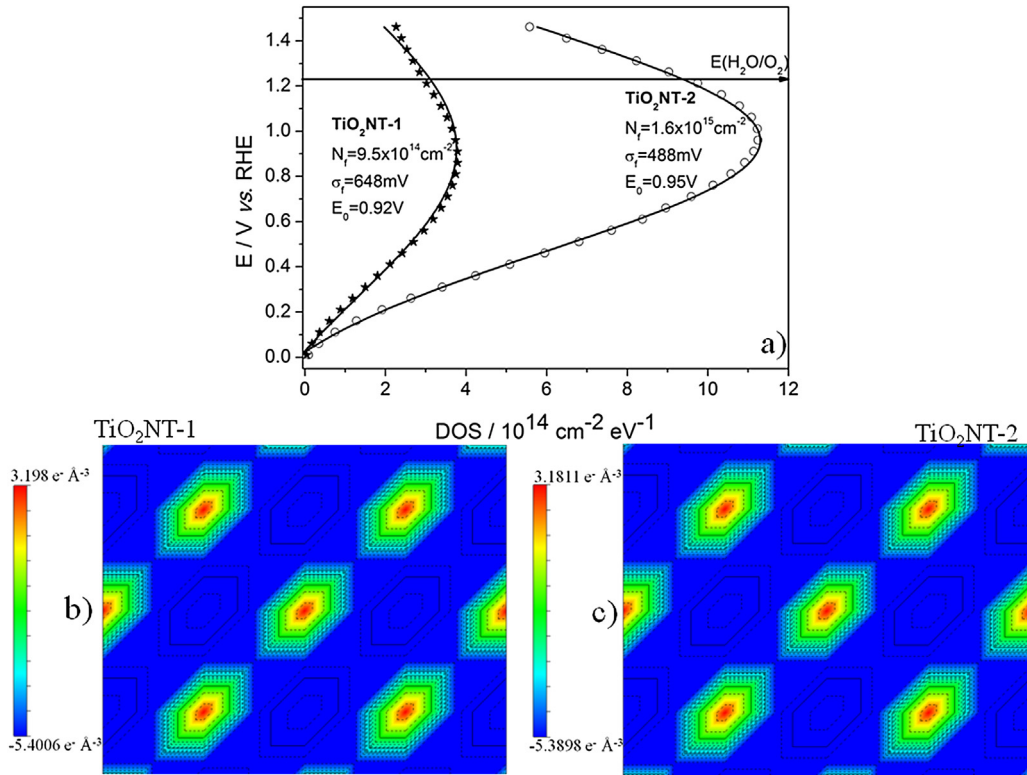


Fig. 8. Density of states as a function of the potential and distribution parameters resulting from fits and electron density maps horizontal plane z-cutting for a) $\text{TiO}_2\text{NT-1}$ and b) $\text{TiO}_2\text{NT-2}$ photoelectrodes.

disorders of $\sigma \cong 50$ meV and larger disorder values of $\sigma \cong 100$ meV have been observed in real devices. The higher energy disorder observed for TiO₂NT-1 when compared to TiO₂NT-2 photoelectrodes could be related to its patch-like bundle morphology (Fig. 1), as well as its higher lattices stress and smaller crystallite size (Fig. 3).

For the crystallite size distribution, the grain boundary results in an energetic barrier, which is translated into resistance, which consequently decreases the photoactivity that can be generated by the cell. However, there are other effects that have received less attention: the near band edges and tail states. The broken periodicity at the grain boundaries introduces states in the gap, and their density will increase with the increase in the material crystallinity disorder.

The energy disorder has a strong influence on a series of kinetic characteristics that control the performance of photodevices: the distribution of localized states, which determine the charge transfer events for electron transfer in exciton dissociation; the motion of electron escape by hopping; and the rate of recombination of electrons and holes. Moreover, the disorder may determine the rate of exciton dissociation at the interface [52], the probability of escape of an electron at the interface from a geminate hole, and the mobility of the electrons at TiO₂NT photoanodes. Garcia-Belmonte and Bisquert [53] simulated the recombination process in photoelectrodes using numerical methods, and observed disorder parameters of 50–100 meV. According to the authors, the disorder parameter significantly influenced the achievable potential. Since $E_{Fn} < E_{mn}$ when derived for low-occupancy conditions, the energy distance of $E_{LUMO} - E_{Fn}$ increases. Similarly, energy losses are related to hole-state occupancy of the donor material. Therefore, narrow disorder involves a reduction in the energy loss.

Additionally, Fig. 8a shows a difference of 1.5 orders of magnitude for TiO₂NT-1 (9.5×10^{14} cm⁻²) when compared to TiO₂NT-2 (1.6×10^{15} cm⁻²) photoanodes. According to Bisquert et al. [54], when comparing two fullerene materials with higher and lower numbers of state densities and the same properties of LUMO level, recombination rate, etc., the first one will produce a higher photoactivity because the E_{Fn} will increase more for a given number of carriers received. Therefore, as is shown in Figs. 5 and 6, the photoactivity for the water splitting reaction over TiO₂NT-2 was remarkably increased.

The precise location of the exponential distribution of the traps in the nanostructured TiO₂ has not yet been established. Howe and Gratzel [55] studied the electron trapping process in colloidal TiO₂ nanoparticles using an electron paramagnetic resonance technique. According to these authors, there are few traps within an isolated TiO₂ nanoparticle. When they are made into a nanocrystalline film, the necking between the particles affects their electronic structure. Therefore, it is very plausible that these traps are primarily located at the sites of particle–particle contact. In addition, Ti⁴⁺ surface states could act as electron traps. However, the energy of the latter states depends on the surface protonation and may be raised into the conduction band by dye adsorption or proton removal. Therefore, their role as an electron trap is questionable.

The annealing procedure in TiO₂ nanostructures can lead to point defects in the crystal lattice, which can lead to x cation vacancies. Therefore, the non-stoichiometric Ti_{1-x}O₂ can be obtained. There are several point defect in a crystal lattice such as Frenkel, Schottky, Wigner, antisite and Stone–Thrower–Wales defect [56]. Among them, Frenkel and Schottky are normally observed. During annealing, the point defects are created by a change in the position of Ti⁴⁺, which migrates through the interstitial sites (Frenkel defects) to occupy lattice vacancies. They can also be formed by the migration of Ti⁴⁺ from the bulk lattice sites (Schottky defect) to the lattice sites on the surface of the crystal

[56]. This cation migration generates a repositioning of the charge distribution in the crystal, which can be illustrated by the electron density maps of Fourier, such as those shown in Fig. 8b and c for TiO₂NT-1 and -2, respectively. Although the nature of point defect is beyond the scope of this paper, it does not hinder the study of DOS. Those DOS (Fig. 8b and c) were obtained using Rietveld Refinement [7–9].

Fig. 8b and c shows that there was the formation of a covalent bond between Ti and the adjacent O. This Figure shows a z-slab where it is possible to observe the x- and y-axis of the grid related to the *a* and *b* lattice parameter. Although the electron density maps of Fourier look similar, there is a decrease in the depth values along z-axis for TiO₂NT-1 ($\rho = 8.5986$ e⁻ Å⁻³) near 30 meV when compared to TiO₂NT-2 ($\rho = 8.5709$ e⁻ Å⁻³), as shown in Fig. 8b and c, respectively. Because the electronegativity of O (non-metal, 3.44 P. u.) is stronger than Ti (metal, 1.54 P.u.), the electron density is localized mostly on the O atom, indicating some electron transfer from the Ti to O atoms. Therefore, O atoms in the TiO₂ lattice form strong bonds and have some covalent character. However, this trend is lower in Fig. 8c when compared to Fig. 8b, once that it is possible to notice that the electron density decreased ~30 meV. Therefore, the strong tendency for oxygen binding in TiO₂NT-1 (Fig. 8b) will result in decreased electron mobility [57], and so, lower photoelectroactivity for water splitting reaction, as observed in Figs. 5–7. Gogotsi et al. [57] studied the coupling of Cr and N in Cr–N-doped TiO₂ using density functional theory. According to the authors, Cr–N coupling decreased the amount of Ti³⁺ in N-doped TiO₂, which might be responsible for the increased photocatalytic activity. In fact, it has been recently reported that Ti³⁺ states are responsible for exciton-like trap states, which limit the electron mobility in TiO₂ nanotubes [58].

It was observed in the present paper that an increase in temperature leads to higher crystallite size and decreased lattice strain. It results in higher photoactivity for the water splitting reaction.

4. Conclusions

The TiO₂NTs synthesized at the higher anodization temperature had lower band-gap values, higher crystallite sizes, and lower lattice strains. The decrease in the boundary crystallite region was associated with recombination centers of photogenerated charge carriers, which increased the water splitting photoactivity. The increase in the apparent roughness was associated with the increase in the anodic photocurrent for TiO₂NT photoelectrodes. Finally, electronic factors, such as the DOS and electron density maps of Fourier, could be modulated.

Acknowledgments

The authors would like to thank the Brazilian Research Funding Institutions CNPq, CAPES, and FAPESP (2010/05555-2, 2012/06778-0) for financial support.

References

- [1] M. Kaneko, I. Okura (Eds.), Photocatalysis – Science and Technology. Ch 2 – Photoelectrochemical Process of Semiconductors, Springer-Verlag, Berlin, 2002, p. 11.
- [2] I. Paramasivam, J.M. Macak, T. Selvam, P. Schmuki, *Electrochim. Acta* 54 (2008) 643.
- [3] S.E. John, S.K. Mohapatra, M. Misra, *Langmuir* 25 (2009) 8240.
- [4] H. Wender, A.F. Feil, L.B. Diaz, C.S. Ribeiro, G.J. Machado, P. Migowski, D.E. Weibel, J. Dupont, S.R. Teixeira, *Appl. Mater. Interfaces* 3 (2011) 1359.
- [5] R.G. Freitas, S.G. Justo, E.C. Pereira, *J. Power Sourc.* 243 (2013) 569.
- [6] H. Li, S.K. Martha, R.R. Unocic, H. Luo, S. Dai, J. Qu, *J. Power Sourc.* 218 (2012) 88.
- [7] H.M. Rietveld, *J. Appl. Crystallogr.* 2 (1969) 65.
- [8] A.C. Larson, R.B. von Dreele, *Lab. Rep. LAUR* 86 (2004) 1.

- [9] B.H. Toby, *J. Appl. Crystallogr.* 34 (2001) 210.
- [10] P. Thompson, D.E. Cox, J.B. Hasting, *J. Appl. Crystallogr.* 20 (1987) 79.
- [11] P.W. Stephens, *J. Appl. Crystallogr.* 32 (1999) 281.
- [12] N.H. March, *Electron Density Theory of Atoms and Molecules*, Academic Press, New York, 1992. Chap. 1.
- [13] H.Y. Hwang, A.A. Prabu, D.Y. Kim, K.J. Kim, *Sol. Energy* 85 (2011) 1551.
- [14] T.T. Isimjan, S.R. Rohani, A.K. Ray, *Int. J. Hydrogen Energy* 37 (2012) 103.
- [15] M. Altomare, M. Pozzi, M. Allieta, L.G. Bettini, E. Sellì, *Appl. Catal. B Environ.* 136 (2013) 81.
- [16] A. Mohammadpour, P.R. Waghmare, S.K. Mitra, K. Shankar, *ACS Nano* 12 (2010) 7421.
- [17] X. Xiao, K. Ouyang, R. Liu, J. Liang, *Appl. Surf. Sci.* 225 (2009) 3659.
- [18] C. Xue, F. Zhang, S. Chen, Y. Yin, C. Lin, *Mat. Sci. Semicond. Process* 14 (2011) 157.
- [19] J.M. Macak, P. Schmiki, *Electrochim. Acta* 52 (2006) 1258.
- [20] Z.B. Xie, D.J. Blackwood, *Electrochim. Acta* 56 (2010) 905.
- [21] H. Liu, L. Tao, W.Z. Shen, *Electrochim. Acta* 56 (2011) 3905.
- [22] D.L. Wood, J. Tauc, *Phys. Rev. B* 5 (1972) 3144.
- [23] R. Asahi, Y. Taga, W. Mannstadt, A.J. Freeman, *Phys. Rev. B* 61 (2000) 7459.
- [24] Z.Y. Wu, G. Ouvrared, P. Gressier, C.R. Natoli, *Phys. Rev. B* 55 (1997) 10382.
- [25] S. Zheng, L. Gao, Q.H. Zhang, J. Sun, *J. Solid State Chem.* 162 (2001) 138.
- [26] G.A. Grimes, G.K. Mor, *TiO₂ Nanotubes: Synthesis, Properties and Applications*, Springer, New York, 2009, p. 90.
- [27] S.H. Kang, J.Y. Kim, Y. Kim, H.S. Kim, Y.E. Sung, *J. Phys. Chem. C* 111 (2007) 9614.
- [28] N.R. Mathew, E.R. Morales, M.A.C. Jacome, J.A.T. Antonio, *Sol. Energy* 83 (2009) 1499.
- [29] Y. Shao, D. Tang, J. Sun, Y. Lee, W. Xiong, *China Part 2* (2004) 119.
- [30] Q. Gao, X. Wu, Y. Fan, *Dyes Pigments* 95 (2012) 96.
- [31] P. Bose, S.K. Pradhan, S. Sen, *Mater. Chem. Phys.* 80 (2003) 73.
- [32] H. Dutta, P. Sabu, S.K. Pradhan, M. De, *Mater. Chem. Phys.* 77 (2002) 153.
- [33] N. Jagtap, M. Bhagwat, P. Awati, V. Ramaswamy, *Thermochim. Acta* 427 (2005) 37.
- [34] Y.C.M. Li, *Thermochim. Acta* 476 (2008) 1.
- [35] M.S. Sikora, A.V. Rosario, E.C. Pereira, C.O.P. Santos, *Electrochim. Acta* 56 (2011) 3122.
- [36] V. Sharma, P. Kumar, N. Singh, S. Upadhyay, V.R. Satsangi, S. Dass, R. Shrivastav, *Int. J. Hydrogen Energy* 37 (2012) 12138.
- [37] A.G. Munoz, *Electrochim. Acta* 52 (2007) 4167.
- [38] L.Y. Lin, C.Y. Chen, M.H. Yeh, K.W. Tsai, C.P. Lee, R. Vittal, C.G. Wu, K.C. Ho, *J. Power Sourc.* 243 (2013) 535.
- [39] J. Bisquert, *J. Phys. Chem. B* 106 (2002) 325.
- [40] M.C. Menard, A.C. Marscholik, K.J. Takeuchi, E.S. Takeuchi, *Electrochim. Acta* 94 (2013) 320.
- [41] H. Zhao, X. Chen, J. Lu, H. Shu, W. Lu, *Solid State Commun.* 166 (2013) 1.
- [42] C.H. Hu, Y. Zhang, H.Y. Liu, S.Q. Wu, Y. Yang, Z.Z. Zhu, *Comput. Mat. Sci.* 65 (2012) 165.
- [43] J. Jamnik, J. Maier, *Phys. Chem. Chem. Phys.* 3 (2001) 1668.
- [44] J. Bisquert, *Phys. Chem. Chem. Phys.* 5 (2003) 5360.
- [45] J. Bisquert, A. Zaban, M. Greenshtein, I. Mora-Seró, *J. Am. Chem. Soc.* 126 (2004) 13550.
- [46] F. Fabregat-Santiago, I. Mora-Seró, G. García-Belmonte, J. Bisquert, *J. Phys. Chem. B* 107 (2003) 758.
- [47] H. Bassler, *Phys. Status Solidi B* 175 (1993) 15.
- [48] J. Bisquert, G. García-Belmonte, J. García-Canadas, *J. Chem. Phys.* 120 (2004) 6726.
- [49] J. García-Canadas, F. Fabregat-Santiago, H. Bolink, E. Palomares, G. García-Belmonte, J. Bisquert, *Synth. Met.* 156 (2006) 944.
- [50] A. Dieckman, H. Bassler, P.M. Biersenbergs, *J. Chem. Phys.* 99 (1993) 8136.
- [51] Z.G. Yu, D.L. Smith, A. Saxeta, R.L. Martin, A.R. Bishop, *Phys. Rev. B* 63 (2001) 085202.
- [52] S. Barth, D. Hertel, Y.H. Tak, H. Bassler, H.H. Horhold, *Chem. Phys. Lett.* 274 (1997) 165.
- [53] G. García-Belmonte, J. Bisquert, *App. Phys. Lett.* 96 (2010) 113301.
- [54] G. García Belmonte, P.P. Boix, J. Bisquert, M. Lenes, H.B. Bolink, A. La Rosa, S. Filippone, N. Martin, *J. Phys. Chem. Lett.* 1 (2010) 2566.
- [55] R. Howe, M. Gratzel, *J. Phys. Chem.* 89 (1985) 4495.
- [56] C. Kittel, *Introduction to Solid State Physics*, seventh ed., John Wiley and Sons, Inc., New York, 1996. Chap. 18.
- [57] M.E. Kurtoglu, T. Longebach, K. Sohlberg, Y. Gogotsi, *J. Phys. Chem. C* 115 (2011) 17392.
- [58] C. Richter, C.A. Schmuttenmaer, *Nat. Nanotechnol.* 5 (2010) 769.